

Kinematic Lensing - Cosmic Shear Without Shape Noise

ERIC M. HUFF,¹ ELISABETH KRAUSE,² TIM EIFLER,² XIAO FANG,² MATTHEW R. GEORGE,^{3,4} AND DAVID SCHLEGEL⁴

¹*Jet Propulsion Laboratory, California Institute of Technology, Pasadena, CA 91109, USA*

²*Steward Observatory/Department of Astronomy, University of Arizona, 933 North Cherry Avenue, Tucson, AZ 85721, USA*

³*Department of Astronomy, University of California, Berkeley, CA 94720, USA*

⁴*Lawrence Berkeley National Laboratory, 1 Cyclotron Rd., Berkeley, CA 94720*

ABSTRACT

We describe a new method for reducing the shape noise in weak lensing measurements by an order of magnitude. Our method relies on spectroscopic measurements of disk galaxy rotation and makes use of the Tully-Fisher relation in order to control for the intrinsic orientations of galaxy disks. For this new proposed method, so-called Kinematic Lensing (KL), the shape noise ceases to be an important source of statistical error.

We use the COSMOLIKE software package to simulate likelihood analyses for two Kinematic Lensing survey concepts (roughly similar in scale to Dark Energy Survey Task Force Stage III and Stage IV missions) and compare their constraining power to a cosmic shear survey from the Large Synoptic Survey Telescope (LSST). Our forecasts in seven-dimensional cosmological parameter space include statistical uncertainties resulting from shape noise, cosmic variance, halo sample variance, and higher-order moments of the density field. We marginalize over systematic uncertainties arising from photometric redshift errors and shear calibration biases considering both optimistic and conservative assumptions about LSST systematic errors.

We find that even the KL-Stage III is highly competitive with the optimistic LSST scenario, while evading the most important sources of theoretical and observational systematic error inherent in traditional weak lensing techniques. Furthermore, the KL technique enables a narrow-bin cosmic shear tomography approach to tightly constrain time-dependent signatures in the dark energy phenomenon.

Keywords: cosmology: observations — gravitational lensing: weak — methods: observational

1. INTRODUCTION

Weak gravitational lensing has been advertised as a powerful probe of cosmology (e.g. Albrecht et al. 2006; Hoekstra & Jain 2008; Weinberg et al. 2013), and is a major science driver for several ongoing and future surveys, such as the Dark Energy Survey¹, the Kiilo Degree Survey², HyperSuprimeCam³, the Large Synoptic Survey Telescope⁴, Euclid⁵, and the Wide-Field Infrared Survey Telescope⁶. It is the least indirect method avail-

able for constraining the distributions of both dark and luminous matter in the universe. Weak lensing by large-scale structure – termed cosmic shear – promises powerful constraints on both the growth of structure and the expansion history of the Universe.

For cosmic shear, typical fluctuations in the matter density field projected over cosmological distances produce lensing distortions to galaxy ellipticities of order 10^{-3} . The noise (per ellipticity component) resulting from the random intrinsic orientations and ellipticities of shapes, by contrast, is $\sigma_\epsilon \sim 0.26$ (e.g. Chang et al. 2013). In order to detect the cosmic shear signal at high significance, lensing analyses must include faint and poorly-resolved galaxies. This comes at a high cost in increased systematic error, as shear measurements using marginal galaxy images are especially susceptible to calibration biases (c.f. Hirata & Seljak 2003; Massey et al. 2013). For all of these reasons, it is highly desir-

Corresponding author: Eric Huff
Eric.M.Huff@jpl.nasa.gov

¹ <http://www.darkenergysurvey.org/>

² <http://kids.strw.leidenuniv.nl/>

³ <http://www.naoj.org/Projects/HSC/>

⁴ <http://www.lsst.org/lsst/>

⁵ sci.esa.int/euclid/

⁶ <http://wfirst.gsfc.nasa.gov/>

able to control for sources of intrinsic scatter in lensing observables.

Several methods have been proposed for reducing the shape noise using additional observables to infer the unlensed properties of galaxies. Polarization in radio observations provides an estimate of the unlensed position angle (e.g., Brown & Battye 2011). Spatially-resolved kinematic maps carry information about the intrinsic orientation (Blain 2002; Morales 2006). In the context of weak lensing magnification, a scaling relation can be used to predict the unlensed size of a galaxy from other photometric quantities (Bertin & Lombardi 2006; Huff & Graves 2014). This paper presents a novel combination of the latter two approaches, employing minimally-resolved disk galaxy kinematics and the Tully-Fisher scaling relation to estimate both components of shear while suppressing shape noise.

This idea proposed in this paper benefits from the fact that the coming decade is likely to see a considerable increase in the capacity of massively multi-object spectroscopy of galaxies at moderate redshifts. Two such instruments currently under development at the time of this writing include the Prime Focus Spectrograph for the Subaru telescope (Takada et al. 2014) and the DESI spectrograph (Levi et al. 2013). The primary science surveys anticipated for these instruments require spectroscopic target densities of 1 arcmin^{-2} , which is nearly an order of magnitude above the previous generation of spectroscopic surveys (Dawson et al. 2013; Blake et al. 2008).

It is the coincidence between this surge in spectroscopic capacity and the widespread scientific interest in weak lensing that motivates the present work. We forecast the cosmological constraining power of a cosmic shear measurement using a large spectroscopic data set (in combination with high-quality imaging) comparable in size to those expected from the aforementioned multi-object spectrographs. We show that, by using a combination of minimally-resolved disk galaxy kinematics and the Tully-Fisher scaling relation, a spectroscopic weak lensing experiment has the potential to greatly improve on the statistical and systematic errors of conventional lensing measurements.

2. BASIC CONCEPTS

In this section we introduce the fundamental observables and key equations necessary to relate kinematic observables to the lensing signal. We aim to show that the two components of the weak gravitational lensing shear distortion can be inferred directly from images and spectra of an individual galaxy. We note that this does require knowledge of the slope and intercept of the

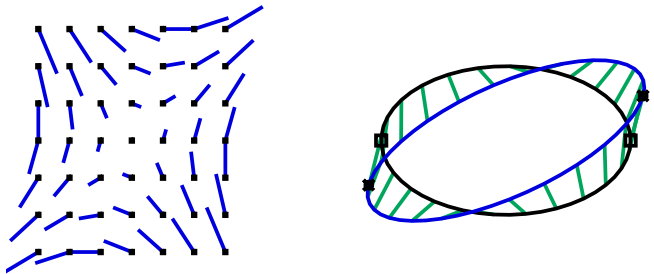


Figure 1. The distortion field (left) produced by a $\gamma_{\times} = 0.2$ shear, and the effect of this distortion on an ellipse (right). Note that the sheared ellipse is not a rotated version of the unsheared because the extremal points of the sheared and unsheared ellipse do not map to one another.

TFR, but this information can be retrieved by fitting the ensemble of observed galaxies.

The reason this is possible can be seen by close inspection of Figure 1. After the shear, the loci originally corresponding to the maximum and minimum of the line-of-sight velocity field (open squares) are no longer located along the apparent major and minor axes of the ellipse, instead appearing at the points indicated by the solid squares. The rotation speed measured along the major axis is always reduced relative to the unsheared case, and the rotation speed measured along the minor axis is always non-zero. *It is thus the difference between the velocity expected from the imaging and the measured velocity field that allows the shear to be inferred for individual galaxies.*

There are two components to the shear, and both can be inferred directly by combining spectroscopy and imaging. We illustrate this further with some simple analytic arguments for measuring the component of the shear aligned with the major axis of galaxy, γ_{+} . The shear component aligned at $\frac{\pi}{4}$ relative to the major axis, γ_{\times} , is treated in the more formal derivation in section 2.1.

Consider the idealized case of an rotationally-supported disk galaxy inclined at some angle i with respect to the observer’s line of sight. This galaxy’s luminosity L and rotation speed (as determined from spectroscopy) v_{spec} are related by the Tully-Fisher Relation (TFR):

$$v_{\text{spec}} = v_{\text{TF}} \sin i \quad (1)$$

where the TFR, relating a stellar mass or absolute magnitude M_B and the disk galaxy’s circular velocity v_{TF} , is commonly parameterized with slope a , pivot M_p , and intercept b as

$$\log v_{\text{TF}} = a \log(M_B + M_p) + b. \quad (2)$$

The rotation speed measured along the *minor* axis is zero, within measurement errors.

Next, we introduce a gravitational lensing signal, applying a shear at some arbitrary angle with respect to the major axis of the galaxy image. Figure 1 shows the result. The lensing distortion re-maps points in the image plane as shown in the left panel, inducing the change in orientation and axis ratio shown in the right panel.

The lensing observables are typically described in terms of the ellipticity, the magnitude of which we define here as

$$e = \frac{1 - q^2}{1 + q^2} \quad (3)$$

where $0 \leq q < 1$ is the semi-minor to semi-major axis ratio of the isophotes of the galaxy image.

The component of the shear aligned with the major axis of the galaxy, γ_+ , transforms the intrinsic (unlensed) ellipticity e_{int} into the observed ellipticity e_{obs} as

$$e_{\text{obs}} = e_{\text{int}} + 2(1 - e_{\text{int}}^2)\gamma_+ \quad (4)$$

(Bernstein & Jarvis 2002).

With only the ellipticity and position angle, it is impossible to tell the difference between the effects of a shear and a change in e_{int} . Wide-field cosmological lensing surveys to date thus need to rely on the fact that the shear is coherent over large length scales, while the intrinsic alignments are, to a good approximation, a shorter-range effect.

The situation changes if v_{spec} is measured and v_{TF} is known. Equation 1 then allows us to directly infer an inclination $\sin i$, and hence an ellipticity e_{spec} from the spectroscopic observables. As is typical when deriving inclination corrections in TFR studies, we assume that $e_{\text{spec}} = e_{\text{int}}$, which allows us to solve Equation 4 directly for the shear.

Note that noise in this relation contributes directly to the intrinsic scatter in the TFR. The latter is constrained by a wide range of observations (Miller et al. 2011; Reyes et al. 2012; Tiley et al. 2016, 2018), which place an upper bound on the scatter between e_{spec} and e_{int} and motivate the shape noise assumed in the forecasts we describe in section 3.1.

What follows is a detailed derivation of the formalism connecting the spectroscopic and imaging observables described above to the cosmological lensing signal.

2.1. The Effect of Shear on Kinematic Observables

In this section, we use toy models of galactic disks to demonstrate how kinemetry can break the degeneracy between shear and shape, controlling for a large fraction of the intrinsic shape noise of disk galaxies. We

show that, to linear order in the shear, γ_+ changes the amplitude of the ellipticity of the galaxy image and γ_\times produces an apparent rotation of said image. That is, γ_\times changes the galaxy ellipse's position angle by θ .

We define the shear as a linear distortion of the image $\mathbf{x}' = \mathcal{A} \mathbf{x}$, where $\mathbf{x} = (x, y)^T$ and $\mathbf{x}' = (x', y')^T$ are the coordinates on the source plane and the image plane, respectively,

$$\mathcal{A} = \begin{pmatrix} 1 + \gamma_+ & \gamma_\times \\ \gamma_\times & 1 - \gamma_+ \end{pmatrix}. \quad (5)$$

We will discuss the effects of lensing on a idealized, circular rotating disk galaxy, with finite edge-on aspect ratio q_z . We choose our coordinate system for the shear distortion such that positive γ_+ induces a shear along the major axis of the galaxy, which means the shape of the unlensed galaxy can be described by an ellipse

$$q^2 x^2 + y^2 = 1. \quad (6)$$

Under the lensing transformation \mathcal{A} and keeping terms up to the first order in shear components, the lensed galaxy becomes

$$q^2(1 - 4\gamma_+)x'^2 + y'^2 - 2(1 + q^2)\gamma_\times x'y' = 1, \quad (7)$$

which is a squeezed (or stretched) and rotated ellipse, comparing to the unlensed galaxy. To see this, let's define an ellipse $q_{\text{obs}}^2 x^2 + y^2 = 1$, where q_{obs} is related to e_{obs} by

$$e_{\text{obs}} = \frac{1 - q_{\text{obs}}^2}{1 + q_{\text{obs}}^2}. \quad (8)$$

We choose our coordinates such that the unlensed galaxy has position angle $\theta_{\text{int}} = 0$; after rotating the galaxy by the observed position angle θ_{obs}

$$\mathcal{R} = \begin{pmatrix} 1 & \theta_{\text{obs}} \\ -\theta_{\text{obs}} & 1 \end{pmatrix}, \quad (9)$$

we obtain the equation of the rotated ellipse

$$q_{\text{obs}}^2 x'^2 + y'^2 - 2\theta_{\text{obs}}(1 - q_{\text{obs}}^2)x'y' = 1, \quad (10)$$

which matches Eq. (4) with

$$q_{\text{obs}}^2 = q^2(1 - 4\gamma_+), \quad (11)$$

$$\theta_{\text{obs}}(1 - q_{\text{obs}}^2) = (1 + q^2)\gamma_\times. \quad (12)$$

Keeping terms up to the first order in shear components and the rotation angle, we obtain

$$e_{\text{obs}} = e_{\text{int}} + 2(1 - e_{\text{int}}^2)\gamma_+, \quad (13)$$

$$\theta_{\text{obs}} = \frac{\gamma_\times}{e_{\text{int}}}. \quad (14)$$

We can see that at linear order in the shear, the even- and odd-parity components have different effects on the image, but in both cases the shear is degenerate with the parameters of the unlensed ellipse. The observables $(e_{\text{obs}}, \theta_{\text{obs}})$ depend on both $(\gamma_+, \gamma_\times)$ and $(e_{\text{int}}, \theta_{\text{int}})$.

We now show how to break this degeneracy and infer both shear components by combining the observed galaxy shapes with kinematic measurements.

For a disk galaxy with an edge-on aspect ratio $0 < q_z < 1$, the inclination is related to the observed axis ratio q by

$$\sin^2 i = \frac{1 - q^2}{1 - q_z^2}. \quad (15)$$

We can re-arrange this relation and combine it with Eq. (1) to get

$$e_{\text{int}} = \frac{(1 - q_z^2)(v_{\text{spec}}/v_{\text{TF}})^2}{2 - (1 - q_z^2)(v_{\text{spec}}/v_{\text{TF}})^2}. \quad (16)$$

Knowledge of the Tully-Fisher relation and measurement of v_{spec} allows for determination of the intrinsic, unlensed ellipticity e_{int} . We can now rewrite Eq. (13) solving for γ_+

$$\gamma_+ = \frac{e_{\text{obs}} - e_{\text{int}}}{2(1 - e_{\text{int}}^2)} \quad (17)$$

and we note that the rhs is comprised of known quantities.

To sum up, a disk galaxy's line-of-sight velocity offset from the TFR predicts an ellipticity e_{int} . The difference between this ellipticity and that of the observed image is proportional to the weak lensing shear component aligned with the galaxy's major axis γ_+ .

Second, the velocity measured along the minor axis of the sheared ellipse, v'_{minor} , informs us of the rotation angle θ_{obs} , as well as γ_\times . Assume that the point on the minor axis has coordinate $\mathbf{x}'_{\text{minor}} = (\cos \vartheta'_{\text{minor}}, \sin \vartheta'_{\text{minor}})^T$, where $\vartheta'_{\text{minor}} = \pi/2 + \theta_{\text{obs}}$ is the polar angle from the positive x -axis. Before being lensed, the point, at linear order, is located at $(\cos \vartheta, \sin \vartheta)$, i.e.,

$$\mathcal{A}^{-1} \mathbf{x}'_{\text{minor}} = \begin{pmatrix} -\theta_{\text{obs}} - \gamma_\times \\ 1 \end{pmatrix} \simeq \begin{pmatrix} \cos \vartheta \\ \sin \vartheta \end{pmatrix}, \quad (18)$$

which gives $\cos \vartheta = -\theta_{\text{obs}} - \gamma_\times = -\gamma_\times(1 + 1/e_{\text{int}})$. Note that $\cos \vartheta$ is also related to v'_{minor} by

$$\frac{v'_{\text{minor}}}{v_{\text{TF}}} = \cos \vartheta \sin i, \quad (19)$$

we can solve for γ_\times as

$$\begin{aligned} \gamma_\times &= -\frac{\cos \vartheta}{1 + 1/e_{\text{int}}} \\ &= -\frac{1}{1 + 1/e_{\text{int}}} \frac{v'_{\text{minor}}}{v_{\text{TF}}} \sqrt{\frac{(1 - q_z^2)(1 + e_{\text{int}})}{2e_{\text{int}}}} \\ &= -\frac{v'_{\text{minor}}}{v_{\text{TF}}} \sqrt{\frac{(1 - q_z^2)e_{\text{int}}}{2(1 + e_{\text{int}})}}. \end{aligned} \quad (20)$$

It can be verified that the effects of γ_+ on the minor axis, and the effects of γ_\times on the major axis are both of quadratic order (see [Bernstein & Jarvis 2002](#), section 2.2).

3. A TULLY-FISHER WEAK LENSING SURVEY

3.1. Effective Shape Noise

We estimate the effective shape noise that would arise from a hypothetical TF lensing experiment by generating catalogs of mock observables with appropriate noise properties. Each quantity in Eqs. 17 and 20 is generated according to the following procedure, with all parameters drawn from [Reyes et al. \(2012\)](#):

1. An absolute magnitude M_B for each mock catalog entry is drawn from a normal distribution with mean -20.5 and standard deviation of unity.
2. For each mock catalog entry, $\log_{10} v_{\text{circ}}$ is drawn from a Gaussian with mean $2.142 - 0.128(M_B + 20.558)$, and a standard deviation (modeling the intrinsic TFR scatter) of $\sigma_{\text{int}} = 0.033$.
3. The cosine of the inclination angle i is drawn uniformly from $[0, 1]$, and the image axis ratio q is assigned as per Eq. 15.

Both shear responses in Eqs. (17,20) are quite sensitive to the line-of-sight orientation of the galaxy in question, suggesting that there are substantial gains to be had from weighting a shear estimate accordingly. Here we calculate the effective shape noise, weighting by each galaxy's observables' shear sensitivity:

$$R_+ = 2(1 - e_{\text{int}}^2) \quad (21)$$

$$R_\times = \sqrt{\frac{2}{1 - q_z^2} \frac{1 + e_{\text{int}}}{e_{\text{int}}}} \quad (22)$$

We calculate the weighted standard deviation in recovered shears for both shear components from our monte-carlo draws using the above procedure, and find values of $\sigma_+ = 0.038$ and $\sigma_\times = 0.014$. We adopt the geometric average for our estimate of the effective shape noise, which yields $\sigma_{\epsilon, \text{TF}} = 0.023$. It should be noted

that this number assumes that the kinematic measurements are dominated by the intrinsic Tully-Fisher and internal disk kinematic dispersions; we defer the modeling the impact of realistic measurement effects to future work. [de Burgh-Day et al. 2015](#), who attempt a similar forecast for shear dispersion using more detailed simulations of the measurement, also find few-percent level shear estimation errors.

LSST-equivalent levels of shape noise should be achievable using kinematics with spectra for 0.4 galaxies per square arcminute. This is comparable to the target densities planned for the next generation of large spectroscopic surveys, and while the instruments currently under construction for these surveys have not been designed to obtain the spatially-resolved spectroscopy necessary for a spectroscopic lensing survey, they may be capable of the measurements discussed here. We discuss this point in general terms in Sect. 3.2.1, but defer instrument-specific survey considerations to a later analysis.

3.2. Designing a Tully-Fisher Lensing Survey

Here we describe two TF survey concepts. The first (hereafter TF-Stage III) is intended to be representative of an experiment that could be performed with instruments similar to those currently under development, relies on optical spectroscopy to measure rotation curves, and covers 5,000 square degrees. The second (hereafter TF-Stage IV) is intended to represent a more optimistic future survey, and assumes a greater redshift reach (which will require an infrared spectrograph) and a survey area of 15,000 square degrees, which is similar to the planned LSST footprint after masking ([Chang et al. 2013](#)).

We estimate the number and redshift distribution of viable targets for each of these two surveys with the Cosmos Mock Catalog (CMC) ([Jouvel et al. 2009](#)). The CMC, created using data from COSMOS⁷, zCOSMOS ([Lilly et al. 2007](#)), and GOODS-N⁸, was designed specifically for tuning target selection criteria for future wide-field imaging and spectroscopic surveys. Spectroscopic templates were fit to the > 500,000 galaxies detected in COSMOS, and the spectral template assignment and luminosity function were validated using zCOSMOS and the deeper GOODS-N imaging, respectively. The CMC has been updated since its original publication; we use the version available on the project website⁹ as of December 2011.

⁷ <http://cosmos.astro.caltech.edu/>

⁸ <http://www.stsci.edu/science/goods/>

⁹ <http://lamwvs.oamp.fr/cosmowiki/RealisticSpectroPhotCat>

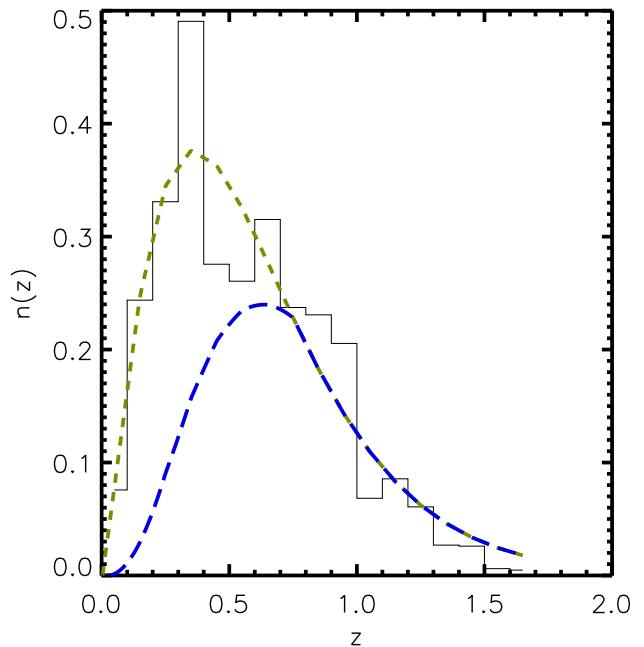


Figure 2. Redshift distributions from the CMC (solid, histogram) for the TF-Stage III experiment. The smooth fit to this is the short-dashed green line, and the redshift distribution used to construct the TF-Stage III covariances is shown in the long-dashed blue line.

For TF-Stage III, we define a viable TF target as one that meets the following criteria:

1. half light radius $\geq 0.5''$
2. r -band magnitude ≤ 23.5
3. morphological template type > 8 (this excludes ellipticals and S0 galaxies)
4. $1,000 \text{ \AA} \leq \lambda_{\text{line}} \leq 10,000 \text{ \AA}$
5. line emission line flux $\geq 10^{-16} \text{ erg s}^{-1} \text{ cm}^{-2}$

We require that at least one of the [OII], [OIII], $H\alpha$, or $H\beta$ emission lines meet both of these criteria. For TF-Stage IV, we extend the spectroscopic window to 20,000Å.

The first two requirements permit detection and shape measurement from photometric catalogs. The third limits the sample to disks, and the fourth to objects with line emission – specifically, line emission that traces the gas disk – in a wavelength range accessible to ground-based spectroscopy. The final requirement ensures that the line emission at 2.2 disk scale lengths be above the

typical sky background at $8,000 \text{ \AA}$ of $10^{-17} \text{ erg s}^{-1}$, and is motivated by previous studies (Miller et al. 2011) which find that rotation curve measurements are most reliable when the emission line is detected out to this distance from the galaxy center. The actual line emission detection threshold will of course depend on the exposure time. Achieving this signal-to-noise ratio should be possible on an 8-m telescope with a PFS-like spectrograph in 30-minute exposures¹⁰, which for this program would entail approximately 4-5 years of dedicated observations.

The available galaxy density set by applying these constraints to the CMC is $2.9/\text{arcmin}^2$. This number is most sensitive to the emission line strength requirement; halving the emission line detection threshold approximately doubles the available target density.

We do not expect a feasible spectroscopic lensing survey to realistically exceed a target density of one galaxy per square arcminute. To construct the redshift distributions for both TF surveys, we first fit a smooth distribution of the usual form:

$$p(z) \propto z^\alpha e^{-(\frac{z}{z_0})^\beta} \quad (23)$$

to the redshift distribution of CMC sources that meet the selection criteria described above. We then subsample this to our fiducial target density assuming that the high-redshift tail is left in place, smoothly reducing the number density at lower redshift in a manner proportional to the comoving volume. The resulting redshift distributions for the CMC selection, its smoothed fit, and the fiducial survey redshift distributions for the TF-Stage III experiment are shown in Fig. 2.

3.2.1. Instrumental Prospects

This paper argues that a TF lensing survey can produce cosmological constraints competitive with other Stage IV dark energy experiments with a sufficient number of spatially resolved disk galaxy spectra. Several wide-field imaging surveys (HSC, LSST, DES) with a weak lensing focus are already planned or underway; we assume that any of these might be used for target selection and shape measurement for a TF survey. The primary obstacle is the collection of order 10^7 resolved spectra.

Two massively multi-object fiber-fed spectroscopic instruments are currently in the advanced planning stage: the Prime Focus Spectrograph for the Subaru telescope (Takada et al. 2014) and the DESI spectrograph

¹⁰ as we are targeting larger, brighter galaxies than the PFS and DESI surveys, the fractional contribution of sky flux to the total flux in each fiber is substantially smaller than for the redshift survey components of those programs.

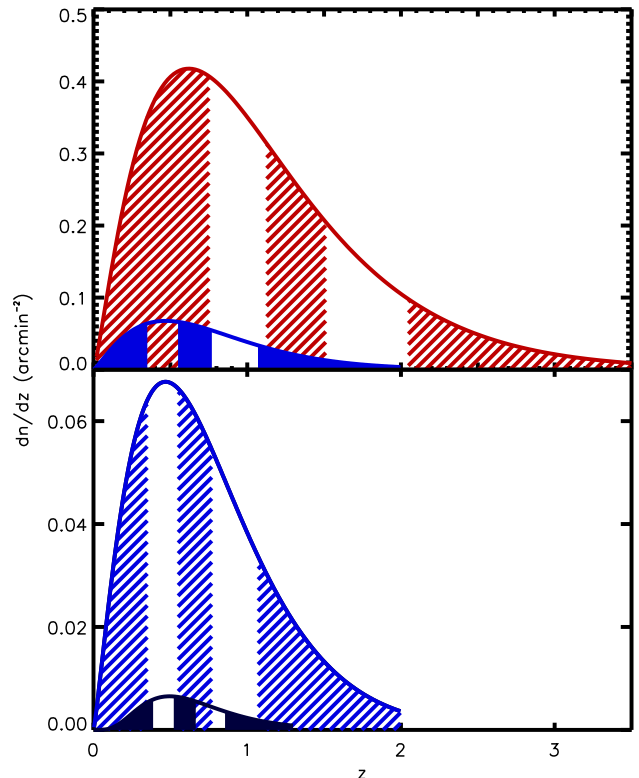


Figure 3. Redshift distributions for our model LSST, DES, and fiducial Tully-Fisher redshift surveys. The top panel shows projections for LSST (red, with line fill) and DES (blue, solid fill). The bottom panel shows DES (blue, line fill) and the TF-Stage III survey (black, solid fill).

(Schlegel et al. 2009). Each is capable of producing target densities in a single exposure of 0.5 per square arcminute. Spatially resolved spectroscopy can in principle be obtained with multiple pointings. DESI, in particular, is planning to collect 50 million galaxy spectra, the majority of which are at $z > 1$. While we defer a more detailed, instrument-specific feasibility study to a future paper, it seems clear that a TF lensing survey is not drastically more challenging than currently planned projects.

4. MODELING COSMOLOGICAL QUANTITIES

We present a side-by-side comparison of a Stage IV Dark Energy experiment (pseudo-LSST) and the proposed Tully-Fisher measurements. In this section, we present a calculation of the expected cosmological constraints from each of these two surveys, including both statistical and systematic error contributions. The following sections describe the prediction code, the systematic errors we consider here, and our method for incorporating the systematics into our model.

4.1. Prediction Code

The simulated likelihood analysis in this paper is computed using the cosmic shear module of COSMOLIKE (Krause & Eifler 2017), which has been used in several ongoing data analysis as well as forecasting efforts of future surveys (Eifler et al. 2014, 2015; Krause et al. 2016; Schaan et al. 2017; Krause et al. 2017; DES Collaboration et al. 2017; Doré et al. 2018). We use the fastest version of COSMOLIKE, which computes the linear power spectrum using the Eisenstein & Hu (1999) transfer function and model the non-linear evolution of the density field as described in Takahashi et al. (2012). We compute time-dependent dark energy models ($w = w_0 + (1 - a)w_a$) following the recipe of ICOSMO (Refregier et al. 2011), which in the non-linear regime interpolates Halofit between flat and open cosmological models (please also see Schrabback et al. 2010, for more details).

From the density power spectrum we compute the shear power spectrum as

$$C^{ij}(l) = \frac{9H_0^4\Omega_m^2}{4c^4} \int_0^{\chi_h} d\chi \frac{g^i(\chi)g^j(\chi)}{a^2(\chi)} P_\delta \left(\frac{l}{f_K(\chi)}, \chi \right), \quad (24)$$

with l being the 2D wave vector perpendicular to the line of sight, χ denoting the comoving coordinate, χ_h

is the comoving coordinate of the horizon, $a(\chi)$ is the scale factor, and $f_K(\chi)$ the comoving angular diameter distance.

The lens efficiency g^i is defined as an integral over the redshift distribution of source galaxies $n(\chi(z))$ in the i^{th} tomographic interval

$$g^i(\chi) = \int_\chi^{\chi_h} d\chi' n^i(\chi') \frac{f_K(\chi' - \chi)}{f_K(\chi')}. \quad (25)$$

Since we chose five tomographic bins, the resulting data vector which enters the likelihood analysis consists of 15 tomographic shear power spectra, each with 20 logarithmically spaced bins ($l \in [30; 5000]$), hence 300 data points overall. In the following analysis we assume different redshift distributions (depending on the probe/survey considered), however we always choose five tomography bins with equal number densities in each z -bin.

4.2. Statistical Covariances

Under the assumption that the shear field is Gaussian (which means that the shear 4pt-function can be expressed in terms of 2pt-functions) the covariance of projected shear power spectra can be expressed as (Hu & Jain 2004)

$$\text{Cov}_G(C^{ij}(l_1)C^{kl}(l_2)) = \langle \Delta C^{ij}(l_1) \Delta C^{kl}(l_2) \rangle = \frac{2\pi \delta_{l_1 l_2}}{A_{l_1} \Delta l_1} [\bar{C}^{ik}(l_1) \bar{C}^{jl}(l_1) + \bar{C}^{il}(l_1) \bar{C}^{jk}(l_1)], \quad (26)$$

with

$$\bar{C}^{ij}(l_1) = C^{ij}(l_1) + \delta_{ij} \frac{\sigma_\epsilon^2}{n^i}, \quad (27)$$

where the superscripts indicate the redshift bin and n^i is the density of source galaxies in the i^{th} redshift bin.

Since non-linear structure growth at late time induces significant non-Gaussianities in the shear field Eq. 26 underestimates the error on cosmological parameters

and needs to be amended by an additional term, i.e. $\text{Cov} = \text{Cov}_G + \text{Cov}_{\text{NG}}$. The non-Gaussian covariance is calculated from the convergence trispectrum T_κ (Cooray & Hu 2001; Takada & Jain 2009), and we include a sample variance term $T_{\kappa, \text{HSV}}$ which describes scatter in power spectrum measurements due to large scale density modes (Takada & Bridle 2007; Sato et al. 2009),

$$\text{Cov}_{\text{NG}}(C^{ij}(l_1), C^{kl}(l_2)) = \int_{|\mathbf{l}| \in l_1} \frac{d^2 \mathbf{l}}{A(l_1)} \int_{|\mathbf{l}'| \in l_2} \frac{d^2 \mathbf{l}'}{A(l_2)} \left[\frac{1}{\Omega_s} T_{\kappa, 0}^{ijkl}(\mathbf{l}, -\mathbf{l}, \mathbf{l}', -\mathbf{l}') + T_{\kappa, \text{HSV}}^{ijkl}(\mathbf{l}, -\mathbf{l}, \mathbf{l}', -\mathbf{l}') \right]. \quad (28)$$

The convergence trispectrum $T_{\kappa, 0}^{ijkl}$ is, in the absence of finite volume effects, defined as

$$T_{\kappa, 0}^{ijkl}(\mathbf{l}_1, \mathbf{l}_2, \mathbf{l}_3, \mathbf{l}_4) = \left(\frac{3}{2} \frac{H_0^2}{c^2} \omega_m \right)^4 \int_0^{\chi_h} d\chi \left(\frac{\chi}{a(\chi)} \right)^4 g^i g^j g^k g^l \times \chi^{-6} T_{\delta, 0} \left(\frac{\mathbf{l}_1}{\chi}, \frac{\mathbf{l}_2}{\chi}, \frac{\mathbf{l}_3}{\chi}, \frac{\mathbf{l}_4}{\chi}, z(\chi) \right), \quad (29)$$

with $T_{\delta, 0}$ the matter trispectrum (again, not including finite volume effects), and where we abbreviated $g^i = g^i(\chi)$.

We model the matter trispectrum using the halo model (Seljak 2000; Cooray & Sheth 2002), which assumes that

all matter is bound in virialized structures that are mod-

eled as biased tracers of the density field. Within this model the statistics of the density field can be described by the dark matter distribution within halos on small scales, and is dominated by the clustering properties of halos and their abundance on large scales. In this model, the trispectrum splits into five terms describing the 4-point correlation within one halo (the *one-halo* term T^{1h}), between 2 to 4 halos (*two-, three-, four-halo* term), and a so-called halo sample variance term T_{HSV} , caused by fluctuations in the number of massive halos within the survey area,

$$T = T_0 + T_{\text{HSV}} = [T_{1h} + T_{2h} + T_{3h} + T_{4h}] + T_{\text{HSV}}. \quad (30)$$

The *two-halo* term is split into two parts, representing correlations between two or three points in the first halo and two or one point in the second halo. As halos are the building blocks of the density field in the halo approach, we need to choose models for their in-

ternal structure, abundance and clustering in order to build a model for the trispectrum. Our implementation of the one-, two- and four-halo term contributions to the matter trispectrum follows Cooray & Hu (2001), and we neglect the three-halo term as it is subdominant compared to the other terms at the scales of interest for this analysis. Specifically, we assume NFW halo profiles (Navarro et al. 1997) with the Bullock et al. (2001) fitting formula for the halo mass–concentration relation $c(M, z)$, and the Sheth & Tormen (1999) fit functions for the halo mass function $\frac{dn}{dM}$ and linear halo bias $b(M)$, neglecting terms involving higher order halo biasing. Within the halo model framework, the halo sample variance term is described by the change of the number of massive halos within the survey area due to survey-scale density modes; following Sato et al. (2009) it is calculated as

$$\begin{aligned} T_{\kappa, \text{HSV}}^{ijkl}(\mathbf{l}_1, -\mathbf{l}_1, \mathbf{l}_2, -\mathbf{l}_2) &= \left(\frac{3 H_0^2}{2 c^2} \Omega_m\right)^4 \times \int_0^{\chi_h} d\chi \left(\frac{d^2 V}{d\chi d\Omega}\right)^2 \left(\frac{\chi}{a(\chi)}\right)^4 g^i g^j g^k g^l \\ &\times \int dM \frac{dn}{dM} b(M) \left(\frac{M}{\bar{\rho}}\right)^2 |\tilde{u}(l_1/\chi, c(M, z(\chi)))|^2 \\ &\times \int dM' \frac{dn}{dM'} b(M') \left(\frac{M'}{\bar{\rho}}\right)^2 |\tilde{u}(l_2/\chi, c(M', z(\chi)))|^2 \\ &\times \int_0^\infty \frac{k dk}{2\pi} P_\delta^{\text{lin}}(k, z(\chi)) |\tilde{W}(k\chi\Theta_s)|^2. \end{aligned} \quad (31)$$

5. SIMULATED LIKELIHOOD ANALYSES

COSMOLIKE computes the analytic covariance and the data vector from a fiducial cosmology (see Table 1) as described in Sect. 4. We assume the covariance to be known, implying that it is fixed with respect to cosmological parameters. This choice can influence cosmological constraints (Eifler et al. 2009); however given that we sample a relatively limited parameter space, especially for our most important comparison (LSST optimistic vs. TF-Stage IV), we believe that it will not change our results qualitatively. We point out that data analyses from the high precision Stage IV surveys require an improved handling of theoretical uncertainties (e.g., Krause & Hirata 2010); however since the data vector is created internally in COSMOLIKE we can exclude these terms in the data and model vector.

In the simulated analysis we sample a seven dimensional cosmological parameter space with flat priors at the boundaries of the parameter range (see Table 1). We

Table 1. Fiducial cosmology and range of cosmological parameters used in the likelihood analyses

	Ω_m	σ_8	n_s	w_0	w_a	Ω_b	h_0
Fiducial	0.315	0.829	0.9603	-1.0	0.0	0.049	0.673
Min	0.1	0.6	0.85	-2.0	-2.5	0.04	0.6
Max	0.6	0.95	1.06	0.0	2.5	0.055	0.76

compare four different surveys (see Table 2 for the exact parameters); two purely photometric surveys mimicking DES and LSST and two versions of the Tully Fisher Lensing surveys, TF-Stage III and TF-Stage IV. For LSST we additionally consider an optimistic and a conservative systematics scenario.

The design of the Tully Fisher Lensing surveys is detailed in Sect. 3; the number density of galaxies for TF-Stage III and TF-Stage IV ($1.1/\text{arcmin}^2$) is limited by

the number of spectra that can be acquired. The survey parameters that we assume in the analyses are summarized in Table 2. Please note that throughout

Table 2. Survey parameters

Survey	area [deg ²]	σ_ϵ	n_{gal}	z_{max}	z_{mean}	z_{med}
TF-Stage III	5,000	0.021	1.1	1.68	0.90	0.73
TF-Stage IV	15,000	0.021	1.1	3.85	1.09	0.84
DES ^a	5,000	0.26	10	2.0	0.84	0.63
LSST ^b	15,000	0.26	31	3.5	1.37	0.93

^aValues taken from DES documents and internal communication within the DES collaboration.

^bValues match specifications outlined in Chang et al. (2013).

the paper σ_ϵ refers to the shape noise per component of the ellipticity.

5.1. Systematic Uncertainties

In addition to the seven cosmological parameters we consider up to seven parameters for photo-z and shear calibration uncertainties. Note that for LSST we consider two different scenarios, termed conservative and optimistic, which differ in the range of photo-z and shear calibration uncertainty prior. The LSST optimistic scenario assumes major breakthroughs in photo-z and shape measurement methods compared to the current state of the art, while the conservative scenario only assumes modest progress.

5.1.1. Photometric Redshifts

In a photometric survey, galaxies are grouped into tomographic bins by their photometric redshifts z_{phot} . To account for the degradation due to uncertainties in the photometric redshift estimates, we compute the true underlying redshift distribution $n_i(z)$ of galaxies in tomography bin $z_{\text{ph}}^i < z_{\text{ph}} < z_{\text{ph}}^{i+1}$ as

$$n^i(z) = \int_{z_{\text{ph}}^i}^{z_{\text{ph}}^{i+1}} dz_{\text{ph}} n(z) p(z_{\text{ph}}|z) \quad (32)$$

using a simple parameterization from Ma et al. (2006) to model $p(z_{\text{ph}}|z)$, the distribution of photometric redshifts given true redshift,

$$p(z_{\text{ph}}|z) = \frac{1}{\sqrt{2\pi}\sigma_z(z)} \exp \left[-\frac{(z - z_{\text{ph}} - z_{\text{bias}}(z))^2}{2\sigma_z^2(z)} \right] \quad (33)$$

i.e. a Gaussian distribution with rms σ_z and offset z_{bias} from the true redshift (but see Hearin et al. 2010 for discussion of critical outliers). We assume photometric redshift estimates to be unbiased on average ($\langle z_{\text{bias}} \rangle = 0$)

and marginalize over the uncertainty of the width of the distribution $\Delta\sigma_z$ and the uncertainty of the redshift bias Δz_{bias} assuming Gaussian distributions with parameter values listed in Table 3.

Since the TF surveys require spectra from each galaxy we assume no error from redshift uncertainty for these.

5.1.2. Shear Calibration Biases

In addition to photo-z uncertainties we consider multiplicative shear calibration bias in the analyses, which we implement as prefactors of the modeled shear power spectra, i.e. $\mathcal{M}^i \mathcal{M}^j C^{ij}(l)$. The superscripts i, j correspond to the tomography bins. We model shear calibration uncertainties as a Gaussian PDF around a fiducial value of 1 and we further assume that the PDFs vary independently in each tomography bin; hence we use five additional parameters to model shear calibration (see Table 3 for parameter ranges). Shear calibration uncer-

Table 3. Systematic error uncertainty parameters

Survey	σ_z	$\Delta\sigma_z$	Δz_{bias}	$\Delta\mathcal{M}$
TF-Stage III	-	-	-	0.0032
TF-Stage IV	-	-	-	0.0016
DES	$0.1(1+z)$	$0.1 \times \sigma_z$	0.01	0.02
LSST, conservative	$0.05(1+z)$	0.01	0.01	0.01
LSST, optimistic ^a	$0.05(1+z)$	0.002	0.003	0.002

^asee <http://lsst.org/files/docs/Phot-z-plan.pdf> for photo-z uncertainties

tainty affects both photometric and Tully Fisher Lensing surveys; however in the latter case our galaxy sample generally has significantly higher S/N ($S/N \geq 50$). Predicting future progress in shear calibration performance is of course difficult; for current measurements, however, the dominant systematic calibration errors appear to arise from noise rectification bias, which scales as $(S/N)^2$ (Refregier et al. 2012). It seems safe to assume that calibration biases will be reduced by limiting the measurement to bright, well-resolved galaxies, and so we adopt the aforementioned S/N scaling and assume a reduction in $\Delta\mathcal{M}$ by a factor of 6.25 when going from DES/LSST to the TF experiments. We note that for TF-Stage IV we rescale the conservative LSST shear calibration uncertainty, not the optimistic one (see Table 3).

5.2. Details of the Analyses and Results

Given the data vector and the covariance COSMO-LIKE samples the parameter space using parallel MCMC

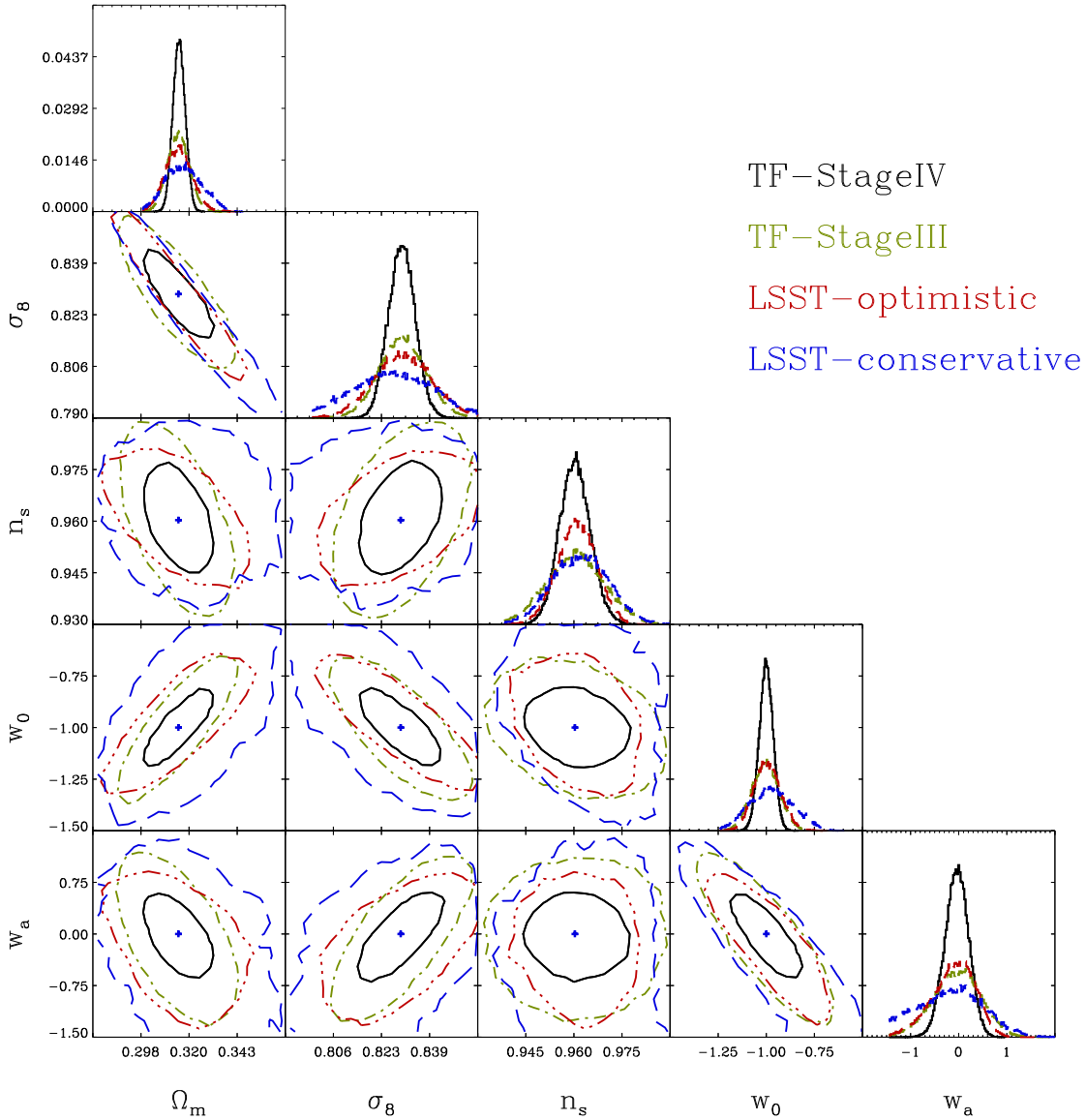


Figure 4. Results of the simulated likelihood analyses. We show the 95% confidence regions for the TF-Stage III survey (black, solid), the TF-Stage IV survey (red, dashed) in comparison with the LSST-optimistic (green, dotted) and pessimistic scenario (blue, dotted-dashed). We marginalize over shear calibration and (for LSST only) photometric redshift systematic errors.

(Goodman & Weare 2010) implemented through the EMCEE python package¹¹. The computing time for the 300-dimensional model vector (including photo- z and multiplicative shear calibration) at each point in parameter space is $\sim 1s$, which in combination with the parallel

MCMC technique allows for an extremely fast sampling of the considered parameter space.

We assume a Multivariate Gaussian being the functional form of the likelihood L ; its width being solely determined by the covariance matrix

$$L(\mathbf{D}|\mathbf{p}_{\text{co}}, \mathbf{p}_{\text{nu}}) \sim \exp\left(-\frac{1}{2} \underbrace{[(\mathbf{D} - \mathbf{M})^t \mathbf{C}^{-1} (\mathbf{D} - \mathbf{M})]}_{\chi^2(\mathbf{p}_{\text{co}}, \mathbf{p}_{\text{nu}})}\right), \quad (34)$$

¹¹ <http://dan.iel.fm/emcee/>

where \mathbf{p}_{co} denotes the cosmological parameter vector, \mathbf{p}_{nu} the nuisance parameter vector, $\mathbf{D} = \mathbf{D}(\mathbf{p}_{\text{co}}^{\text{fid}}, \mathbf{p}_{\text{nu}}^{\text{fid}})$ is the data vector consisting of the 300 $C^{ij}(l)$ that are computed from the fiducial model, $\mathbf{M} = \mathbf{M}(\mathbf{p}_{\text{co}}, \mathbf{p}_{\text{nu}})$ is the corresponding model vector at a given point in cosmological and nuisance parameter space, and \mathbf{C} is the covariance described in Sect. 4.2.

We use Bayes theorem to compute the posterior probability

$$P(\mathbf{p}_{\text{co}}, \mathbf{p}_{\text{nu}} | \mathbf{D}) = \frac{P_r(\mathbf{p}_{\text{co}}, \mathbf{p}_{\text{nu}}) L(\mathbf{D} | \mathbf{p}_{\text{co}}, \mathbf{p}_{\text{nu}})}{E(\mathbf{D})} \quad (35)$$

with E being a normalization called evidence. We assume a flat prior probability P_r in the cosmological parameter space (see Table 1 for details) and Gaussian priors for our nuisance parameters (see Sect. 5.1). For the LSST and the Tully Fisher analyses the priors do not impact the contours at all; for the DES analysis the prior on w_a cuts off outer regions of the corresponding parameter space.

Constraints that are marginalized over nuisance parameters (or cosmological parameters that are not of interest) are calculated as

$$L(\mathbf{D} | \mathbf{p}_{\text{co}}) = \int d\mathbf{p}_{\text{nu}} \exp\left(-\frac{1}{2}\chi^2(\mathbf{p}_{\text{co}}, \mathbf{p}_{\text{nu}})\right). \quad (36)$$

For the final runs of the simulated likelihood analyses we compute 420,000 steps in the MCMC and reject the first 10,000 steps as a burn-in phase. We also run several shorter chains to check for convergence.

We produce a compressed summary of the different experiments by computing a measure of the cosmological information content equal to $\|\Xi\|^{-\frac{1}{n}}$, where n is the number of cosmological parameters of interest, and Ξ is the covariance matrix of the MCMC outputs

$$\Xi_{ij} = \text{cov}(p_{\text{co}i}, p_{\text{co}j}). \quad (37)$$

This information measure corresponds roughly to the geometric average of the constraints on the \mathbf{p}_{co} , or the square of the size of the ball in parameter hyper-space enclosing the $1 - \sigma$ likelihood surface; it is worth noting that this particular measure of experimental merit is insensitive to the number of parameters. Table 5 shows the ratio of this quantity for each of the four surveys considered here to that of the Dark Energy Survey.

For better illustration we also show two-dimensional contour plots for the most interesting cases, i.e. TF-Stage III and TF-Stage IV vs. LSST conservative and optimistic (Fig. 4). These 95% confidence regions are marginalized over all other cosmological parameters (five) and nuisance parameters (five and seven for TF and LSST, respectively).

5.3. Discussion

This analysis makes a number of conservative assumptions which favor photometric weak lensing measurements. We do not include any intrinsic alignment contamination in the LSST or DES cosmic shear forecasts, nor do we allow for the possibility of catastrophic photometric redshift errors. Neither of these effects are present for the TF survey concepts, though both are important limitations of traditional methods (Hirata & Seljak 2004; Hearin et al. 2010). We also assume that the shear calibration biases scale as $(S/N)^2$, despite claims that noise rectification bias, which appear to be the dominant source of shear calibration problems for many existing shape measurement methods, can be removed at this order (Kacprzak et al. 2012). Allowing for a higher order calibration-S/N scaling would further enhance the cosmological information content of the TF surveys. Finally, we have made no attempt to optimize the extraction of 3D lensing information. It is likely that a tomographic analysis using additional redshift bins would further improve the power of the TF-Stage III and TF-Stage IV analyses.

Nevertheless, Fig. 4 and Table 5 show that the TF-Stage III experiment – which would require only an overlapping DESI-like spectrograph and a DES-like imaging survey – is comparable in constraining power to our optimistic LSST forecasts. The TF-Stage IV experiment provides constraining power well in excess of any other optical ground-based lensing measurement and offers a way to break through the information ceiling set for traditional lensing experiments by the surface density of galaxies suitable for shape measurement.

For a better understanding of the individual error contributions we show the correlation matrices of the LSST survey (*left*) and the TF-Stage III survey (*right*) in Fig. 5. As described in Sect. 4.2 our covariance consists of shape noise, cosmic variance (including higher order terms), and halo sample variance. Shape noise and second order cosmic variance act on the diagonal and secondary diagonal only, while halo sample variance and higher order cosmic variance act on all elements of the covariance.

For the LSST survey one can see that the larger shape noise on main and secondary diagonals dominates the submatrices at higher redshift bins and plays an important role for the low- z submatrices as well. Elements that are far from the (secondary) diagonal quickly fall off and become subdominant. In contrast, and as a result of the decreased shape noise term, the TF survey's error budget is clearly dominated by higher order cosmic variance and halo sample variance, as indicated by the large off-diagonal terms.

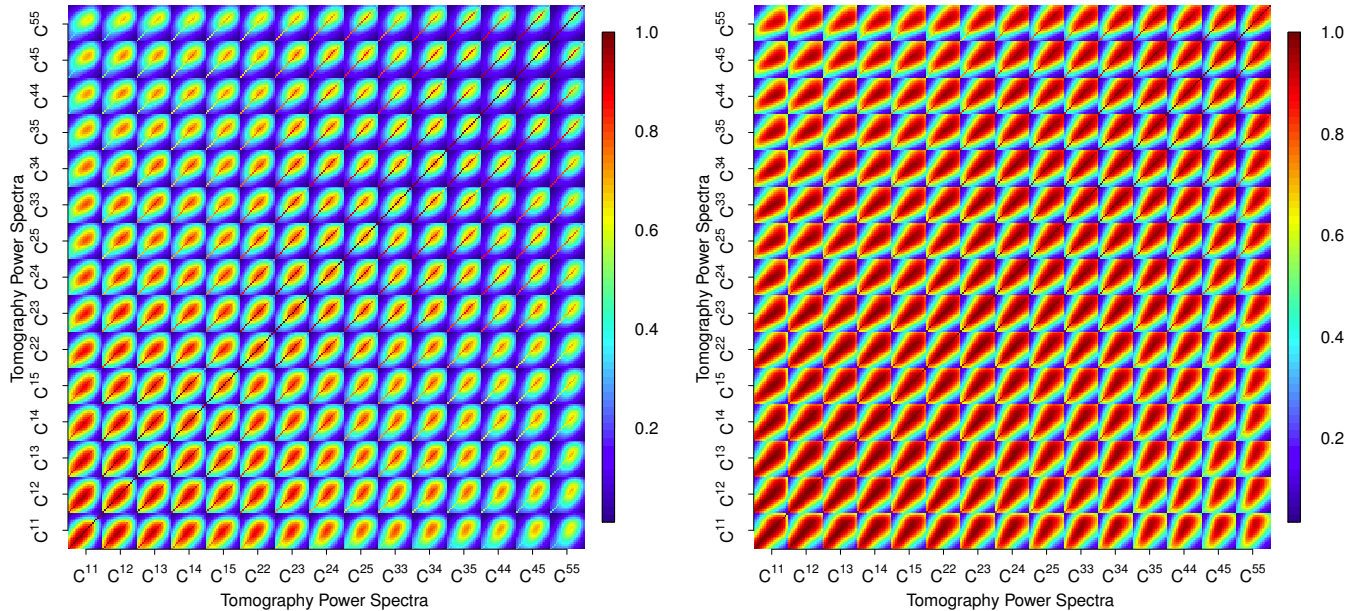


Figure 5. Correlation plots of the LSST covariance (*left*) and the TF covariance (*right*). The data vector consists of 15 tomography power spectra, each with 20 l -bins, i.e. 300 data points altogether. Shape noise only acts on the main and secondary diagonals; see text for further explanation.

Table 4. Marginalized One-Parameter Constraints

Survey	Ω_m	σ_8	n_s	w_0 ,	w_a	H_0
LSST-optimistic	0.016	0.015	0.0097	0.14	0.52	0.030
LSST-conservative	0.020	0.018	0.012	0.25	0.90	0.036
TF-Stage III	0.0011	0.0097	0.012	0.14	0.50	0.037
TF-Stage IV	0.0064	0.0056	0.0065	0.073	0.25	0.026

Table 5. Cosmological Information Content relative to DES

Survey	Information Content (relative to DES)
LSST-pessimistic	2.39
LSST-optimistic	3.31
TF-Stage III	3.60
TF-Stage IV	7.10

This dominance permits an analysis with narrower tomographic bins, which is an extremely powerful tool to explore time-dependent signatures in the dark energy phenomenon and separately constrain expansion history and structure growth.

Regarding the robustness of our TF constraints we point out that an error of the disk circular velocity of 13 km/s is likely a conservative assumption. If instead we assume an error of 10 km/s, which is reason-

ably achievable with today’s instruments already, we can tolerate a $\sim 35\%$ percent failure rate in obtaining the required galaxy spectra while still achieving the constraints shown in Fig. 4.

6. CONCLUSIONS

In this paper we have presented a new method to extract cosmological information from weak gravitational lensing. Using the well-established Tully-Fisher scaling relation we substantially decrease the ellipticity dispersion contribution to the error budget (from ~ 0.26 to ~ 0.02), which is a major limitation of current cosmic shear surveys. To overcome this limitation cosmic shear surveys have to increase the depth of the survey and thereby the number density of galaxies, which in return causes increased photo- z and shear calibration uncertainty associated with the low S/N of these faint galaxies.

The limitation of our method clearly is the need for spectroscopic information and hence the limited num-

ber of galaxies that can be observed spectroscopically within a given time interval. As a result the model surveys we present in this paper (TF-Stage III and TF-Stage IV) have an average number density of galaxies of $1.1/\text{arcmin}^2$, however they are not affected by photo-z uncertainty and only little by shear calibration errors. For our model surveys we adopt the DETF “Stage X” terminology in the sense that TF-Stage III covers $5,000\text{deg}^2$ (similar to DES), and TF-Stage IV covers $15,000\text{deg}^2$ (similar to LSST); also we assume a similar improvement in survey depth when going from Stage III to Stage IV.

Using the cosmic shear module of COSMOLIKE we run various simulated cosmic shear tomography likelihood analyses, in a multi-dimensional parameter space (seven cosmological parameters, and five and two parameters for shear calibration and photo-z errors, respectively). These simulated analyses include full Non-Gaussian covariances and a realistic sampling of the parameter space which is a major improvement over Fisher forecasts.

Our main findings are that already TF-Stage III is competitive with LSST, depending on the assumptions of how strongly nuisance parameters impact the LSST constraints; TF-Stage IV clearly outperforms even the optimistic scenarios for LSST. In this context we mention all LSST analyses assume zero intrinsic alignment contamination, which potentially is of similar importance as photo-z and shear calibration uncertainties.

It is however important to note that any TF-survey obviously relies on overlapping photometric and spectroscopic data, hence the main intention of this comparison is to strongly advocate a spectroscopic survey overlapping with LSST. The interesting prospect of this overlap is not just a TF-Stage IV survey but a combination of TF-Stage IV and LSST. Galaxies without

spectra will substantially contribute to the constraints, especially since the overlap with spectroscopic data allows for improved photo-z and shear calibration and IA mitigation schemes.

Another interesting prospect is the design of an optimal TF-lensing tomographic survey. The small shape noise and the accurate redshift information allows for substantially more tomographic bins and hence for a precise measurement of expansion history vs structure growth. We point out that the TF-lensing method presented in this paper can be applied to cluster lensing, galaxy-galaxy lensing and other cross-lensing probes, thereby overcoming possible limitations of these probes due to shape noise.

Using the TF method presented in this paper cosmic shear for the first time is no longer fundamentally limited by shape noise errors and systematics associated with it but by the instrumental capabilities of multi-object spectrographs.

ACKNOWLEDGMENTS

We thank Klaus Honscheid, David Weinberg, Rachel Mandelbaum, Chris Hirata, Bhuvnesh Jain, and Peter Schneider for very useful discussions and advice. We also thank the Center for Cosmology and Astroparticle Physics at the Ohio State University and the Center for Particle Cosmology at the University of Pennsylvania for hosting us during critical phases of the paper. This paper is based upon work supported in part by the National Science Foundation under Grant No. 1066293 and the hospitality of the Aspen Center for Physics. This research funded in part by by NASA ROSES ATP 17-ATP17-0173.

REFERENCES

- Albrecht, A., Bernstein, G., Cahn, R., et al. 2006, arXiv:astro-ph/0609591, astro-ph/0609591
- Bernstein, G. M., & Jarvis, M. 2002, *AJ*, 123, 583
- Bertin, G., & Lombardi, M. 2006, *ApJL*, 648, L17
- Blain, A. W. 2002, *ApJL*, 570, L51
- Blake, C., Brough, S., Couch, W., et al. 2008, *Astronomy and Geophysics*, 49, 5.19
- Brown, M. L., & Battye, R. A. 2011, *ApJL*, 735, L23
- Bullock, J. S., Kolatt, T. S., Sigad, Y., et al. 2001, *MNRAS*, 321, 559
- Chang, C., Jarvis, M., Jain, B., et al. 2013, *MNRAS*, 434, 2121
- Cooray, A., & Hu, W. 2001, *ApJ*, 554, 56
- Cooray, A., & Sheth, R. 2002, *PhR*, 372, 1
- Dawson, K. S., Schlegel, D. J., Ahn, C. P., et al. 2013, *AJ*, 145, 10
- de Burgh-Day, C. O., Taylor, E. N., Webster, R. L., & Hopkins, A. M. 2015, *PASA*, 32, e040
- DES Collaboration, Abbott, T. M. C., Abdalla, F. B., et al. 2017, ArXiv e-prints, arXiv:1708.01530
- Doré, O., Hirata, C., Wang, Y., et al. 2018, ArXiv e-prints, arXiv:1804.03628
- Eifler, T., Krause, E., Dodelson, S., et al. 2015, *MNRAS*, 454, 2451
- Eifler, T., Krause, E., Schneider, P., & Honscheid, K. 2014, *MNRAS*, 440, 1379

- Eifler, T., Schneider, P., & Hartlap, J. 2009, *A&A*, 502, 721
- Eisenstein, D. J., & Hu, W. 1999, *ApJ*, 511, 5
- Goodman, J., & Weare, J. 2010, *Communications in Applied Mathematics and Computational Science*, 5, 65.
<http://dx.doi.org/10.2140/camcos.2010.5.65>
- Hearin, A. P., Zentner, A. R., Ma, Z., & Huterer, D. 2010, *ApJ*, 720, 1351
- Hirata, C., & Seljak, U. 2003, *MNRAS*, 343, 459
- Hirata, C. M., & Seljak, U. 2004, *PhRvD*, 70, 063526
- Hoekstra, H., & Jain, B. 2008, *Annual Review of Nuclear and Particle Science*, 58, 99
- Hu, W., & Jain, B. 2004, *PhRvD*, 70, 043009
- Huff, E. M., & Graves, G. J. 2014, *The Astrophysical Journal Letters*, 780, L16.
<http://stacks.iop.org/2041-8205/780/i=2/a=L16>
- Jouvel, S., Kneib, J.-P., Ilbert, O., et al. 2009, *A&A*, 504, 359
- Kacprzak, T., Zuntz, J., Rowe, B., et al. 2012, *MNRAS*, 427, 2711
- Krause, E., & Eifler, T. 2017, *MNRAS*, 470, 2100
- Krause, E., Eifler, T., & Blazek, J. 2016, *MNRAS*, 456, 207
- Krause, E., & Hirata, C. M. 2010, *A&A*, 523, A28
- Krause, E., Eifler, T. F., Zuntz, J., et al. 2017, *ArXiv e-prints*, arXiv:1706.09359
- Levi, M., Bebek, C., Beers, T., et al. 2013, *ArXiv e-prints*, arXiv:1308.0847
- Lilly, S. J., Le Fèvre, O., Renzini, A., et al. 2007, *ApJS*, 172, 70
- Ma, Z., Hu, W., & Huterer, D. 2006, *ApJ*, 636, 21
- Massey, R., Hoekstra, H., Kitching, T., et al. 2013, *MNRAS*, 429, 661
- Miller, S. H., Bundy, K., Sullivan, M., Ellis, R. S., & Treu, T. 2011, *ApJ*, 741, 115
- Morales, M. F. 2006, *ApJL*, 650, L21
- Navarro, J. F., Frenk, C. S., & White, S. D. M. 1997, *ApJ*, 490, 493
- Refregier, A., Amara, A., Kitching, T. D., & Rassat, A. 2011, *A&A*, 528, A33+
- Refregier, A., Kacprzak, T., Amara, A., Bridle, S., & Rowe, B. 2012, *MNRAS*, 425, 1951
- Reyes, R., Mandelbaum, R., Gunn, J. E., et al. 2012, *MNRAS*, 425, 2610
- Sato, M., Hamana, T., Takahashi, R., et al. 2009, *ApJ*, 701, 945
- Schaan, E., Krause, E., Eifler, T., et al. 2017, *PhRvD*, 95, 123512
- Schlegel, D. J., Bebek, C., Heetderks, H., et al. 2009, *ArXiv e-prints*, arXiv:0904.0468
- Schrabback, T., Hartlap, J., Joachimi, B., et al. 2010, *A&A*, 516, A63
- Seljak, U. 2000, *MNRAS*, 318, 203
- Sheth, R. K., & Tormen, G. 1999, *MNRAS*, 308, 119
- Takada, M., & Bridle, S. 2007, *New Journal of Physics*, 9, 446
- Takada, M., & Jain, B. 2009, *MNRAS*, 395, 2065
- Takada, M., Ellis, R. S., Chiba, M., et al. 2014, *PASJ*, 66, R1
- Takahashi, R., Sato, M., Nishimichi, T., Taruya, A., & Oguri, M. 2012, *ApJ*, 761, 152
- Tiley, A. L., Stott, J. P., Swinbank, A. M., et al. 2016, *MNRAS*, 460, 103
- Tiley, A. L., Bureau, M., Cortese, L., et al. 2018, *MNRAS*, arXiv:1810.07202
- Weinberg, D. H., Mortonson, M. J., Eisenstein, D. J., et al. 2013, *PhR*, 530, 87